VISUALIZATION OF HYDRODYNAMIC FIELD AND AEROACOUSTIC SOURCE IN TRANSITIONAL JET BY TR-TOMO PIV

D. VIOLATO[1c] AND F. SCARANO[1]

[1]Department of Aerospace Engineering, Delft University of Technology, 2629 HS, Delft, The Netherlands

[c]Corresponding author: Email: D.Violato@tudelft.nl

ABSTRACT: The three-dimensional behavior of flow transition in circular jets at *Re*=5,000 is investigated with experiments conducted on a free water jet by time-resolved tomographic particle image velocimetry. The emphasis is on the unsteady organization of coherent flow structures, which play a role in the generation of acoustic noise. Shedding and pairing of vortices are the most pronounced phenomena observed in the near field. The characteristic pulsatile motion lead to the formation of streamwise vortices and the growth of vortex-ring azimuthal waves. These culminate in the breakdown of the vortex ring by abrupt axial ejection of the azimuthal humps. The proper orthogonal decomposition (POD) is applied to the velocity and the vorticity fields to objectively classify and describe the three-dimensional patterns at transition. The most energetic modes of velocity show helical and precession motion of the jet core, whereas vorticity modes reveal a characteristic orientation of 45 degrees to the jet axis of the radial and the axial components. Following Powell's aeroacoustic analogy, Lamb vector field is analyzed by POD and the instantaneous spatial distribution of the acoustic source term is mapped by the temporal derivative of the Lamb vector, revealing the highest activity during vortex ring breakdown.

1. INTRODUCTION

Acoustic emissions in jet flows are believed to be related to the dynamical behavior of large-scale flow structures and their interactions. Sound radiation originates from vortex pairing (Crow and Champagne, 1971; Schram, 2005) and the collapse of the annular mixing-layer at the end of the potential core (Hussain and Zaman, 1981; Jordan *et al*., 2007). Experimental studies that describe the dynamical behaviour of large-scale structures and their interactions in jets are particularly relevant to investigate the physical mechanism associated with sound production.

Experimental investigations on the organization of coherent flow structures require field measurement techniques such as flow visualization (Dimotakis *et al*., 1983) and, in the last decades, particle image velocimetry (PIV). This was employed along streamwise or cross-sectional planes of the jet to investigate the unsteady behavior of the shear layer and the transition patterns (Liepmann and Gharib, 1992). On the other hand, descriptions of the dynamical behavior and the three-dimensional patterns of flow structures require time-resolved volume-based techniques. The advent of tomographic PIV (TOMO PIV, Elsinga *et al*., 2006) enabled the measurement of the instantaneous velocity vector field over a three-dimensional domain, with the advantage that the complete velocity gradient tensor and the associated quantities (e.g. the vorticity vector and the second invariant) can be obtained also in high-speed flow regimes. For low speed jets, Violato and Scarano (2011) have employed time-resolved tomographic PIV to investigate the evolution of three-dimensional structures in circular and chevron jets.

The role of large-scale coherent structures in circular jets has been the objective of several investigations. In the region next to the nozzle, the fluctuations are organized as vortex rings that generate from the growth of the Kelvin-Helmholtz (K-H) instability. At moderate Reynolds number, such structures grow maintaining axial symmetry and undergo pairing due to the mutual flow induction (Crow and Champagne, 1971; Schram 2005). Further downstream, the flow transition to turbulence occurs with the growth of three-dimensional instabilities, such as azimuthal oscillations of the vortex rings (Yule, 1978). Counter-rotating pairs of streamwise vortices are also reported to exist in the braid region between two vortex rings. By the end of the potential core ring vortices disrupt into coherent substructures (Hussain and Zaman, 1981) and the formation of smaller scales that ejects bursts of fluids (Liepmann and Gharib, 1992).

In the last decade, PIV has been successfully used in combination with aeroacoustic analogies to study the flow-field pattern producing noise. The potential and relevance of this methodology have found acknowledgements in recent review articles (Jordan and Gervais, 2008; Morris, 2011). In a Mach 0.85 jet, Seiner et al. (1999) characterized the noise sources using two-point turbulence statistics to evaluate the Lighthill turbulent stress tensor and observed that the actual measurement of the Lighthill's acoustic tensor requires volumetric measurements with temporal resolution. In a subsonic and acoustically excited jet flow at low Reynolds number, Schram et al. (2005) investigated the mechanism of sound generation by vortex pairing with phase-locked planar PIV and a conservative formulation of vortex sound theory for axisymmetric flow, finding good agreement between the sound prediction and the sound measured by microphone at frequencies not contaminated by the acoustical excitation. Violato and Scarano (2011) showed the need for time-resolved three-dimensional measurements to discuss the relation between the coherent structures and the instantaneous acoustic production based on Powell's analogy (Powell, 1964)

In this work, state-of-the-art experimental capabilities are employed to perform TR-TOMO PIV measurements over a jet axial extent such that to capture the large-scale events from the nozzle to 3-4 jet diameters beyond the end of the potential core. The investigation is conducted under favorable experimental conditions in a water facility, where a relatively large measurement domain can be accessed with TOMO-PIV (Scarano and Poelma, 2009) and where high-speed PIV systems can operate at a repetition such to resolve the smallest flow time scales. The study presents first an analysis of the vortex topology and evolution using the vorticity and the λ_2-criterion (Jeong and Hussain, 1995). Emphasis is focused on the collapse of the annular mixing-layer at the end of the potential core. The proper orthogonal decomposition (POD, Berkooz *et al.*, 1993) is applied to the velocity and vorticity fields to objectively classify and describe the three-dimensional patterns at transition. Finally, following Powell's aeroacoustic analogy, the Lamb vector field is analysed by POD and the relation between the coherent structures and the instantaneous acoustic production is discussed associating the acoustic source to the second-time derivative of the Lamb vector.

2. POD ANALYSIS

Proper Orthogonal Decomposition (POD, Berkooz et al., 1993) is a statistical technique to objectively classifying and describing turbulent flows in terms of most energetic coherent motions that can be used to produce of a low-order reconstruction of the flow field. Any of the velocity snapshots $u(\mathbf{x},t_n)$ can be reconstructed using an arbitrary number of modes, *K*:

$$u(\mathbf{x},t_n) = \overline{u}(\mathbf{x},t_n) + \sum_{k=1}^{K} a_k(t_n)\psi_k(\mathbf{x}) \qquad (1)$$

According to the snapshot POD method (Sirovich, 1987), which is implemented in this study, POD eigenmodes can be written as a linear sum of the data vectors

$$\psi_k(\mathbf{x}) = \sum_{n=1}^{N} \Phi_n^k u'(\mathbf{x},t_n) \quad k = 1,\ldots,N \qquad (2)$$

where Φ_n^k is the n^{th} component of the k^{th} eigenvector and $u'(\mathbf{x},t_n) = u(\mathbf{x},t_n) - \overline{u}(\mathbf{x},t_n)$ is the fluctuating component of the velocity snapshot. The eigenmodes can then be found by solving the following eigenvalue problem

$$C_u \Phi = \lambda \Phi \qquad (3)$$

where C is the L_2-norm matrix,

$$C_u = \frac{1}{N}\left(u'(\mathbf{x}), u'(\mathbf{x})\right) \qquad (4)$$

The cumulative sum of the eigenvalues λ_k corresponds to the total energy and each eigenmode is associated with an energy percentage e_k based on the eigenmode's eigenvalue:

$$e_k = \lambda_k \Big/ \sum_{i=1}^{N} \lambda_i \,. \qquad (5)$$

In this investigation, POD analysis is first conducted on three-dimensional velocity data sets based on the mean square fluctuating energy eq. (4). Then, by centred difference scheme, the velocity information is used to evaluate the three-dimensional vorticity field. This is analysed by POD using, as a norm, the mean square fluctuating enstrophy

$$C_\omega = \frac{1}{N}\left(\omega'(\mathbf{x}), \omega'(\mathbf{x})\right), \qquad (6)$$

where ω' is the fluctuating vorticity. Kostas *et al.* (2005), argued that more efficient identification of the coherent structures in PIV data can be obtained by the vorticity decomposition. Finally, the velocity and the vorticity vectors are used to evaluate the Lamb vector $\mathbf{L}=\boldsymbol{\omega}\times\mathbf{V}$, which is a relevant quantity in aeroacoustics as it accounts for the flow state in Powell's aeroacoustic analogy. The modal analysis of the Lamb vector field is conducted by POD based on the norm of the fluctuating component L' as follows:

$$C_L = \frac{1}{N}\left(L'(\mathbf{x}), L'(\mathbf{x})\right). \qquad (7)$$

3. EXPERIMENTAL APPARATUS AND PROCEDURES

Experiments are conducted in the water jet facility described in Violato and Scarano (2011) at the Aerodynamic Laboratories of TU Delft in the Aerospace Engineering Department. A round nozzle of exit diameter D=10 mm and contraction ratio of 56:1, is installed at bottom wall of an octagonal water tank. The system is hydrostatically driven and provides a stabilized supply in a range of exit velocity W_j from 0.1 to 2m/s, corresponding to Reynolds numbers ranging between 1,000 and 20,000. Tomographic experiments are performed for a nominal axial velocity at the jet exit of 0.5 m/s yielding a Reynolds number Re= 5,000 based on the jet diameter D.

Neutrally buoyant polyamide particles of 56 μm of diameter are dispersed homogeneously, achieving a uniform concentration of 0.65 particles/mm^3. The illumination is provided by a Quantronix *Darwin-Duo* solid-state diode-pumped Nd:YLF laser (2x25 mJ/pulse at 1 kHz). After a transmission distance of 1.5 m, the laser beam, which has a diameter of 6 mm, is expanded through a diverging lens to a diameter of 80 mm and then is focused with a converging lens to obtain a conical illumination (Figure 1). The light scattered by the particles is recorded by a tomographic system composed of three 3 *Imager pro HS 4M* cameras arranged horizontally with azimuthal aperture of 90 degrees. The choice of conical illuminated volume eliminates the need for camera-lens tilt mechanism to comply with the Scheimpflug condition. Nikon objectives of 105 mm focal length are set with a numerical aperture $f_\#$= 22 to allow focused imaging of the illuminated particles. For the chosen illumination and imaging configuration the particle image density decreases towards the edge of the illuminated volume and, at the jet axis, increases along the axial domain between 0.037 and 0.043 particles/pixel. The details of the experimental settings are summarized in table 1. The choice of a conical domain of illumination also results in a more favorable condition for accurate reconstruction of the particle field, as the particle image density does not change with the viewing angle along the azimuth and decreases moving from the axis to the periphery of the jet (Figure 1).

Sequences of images of tracer particles are recorded at 1 kHz resulting in a temporal resolution that yields 35 samples for the fastest expected events (vortex shedding). The imaged-particle displacement at the exit is approximately 10 pixels along the jet axis. The field of view is of 50 x 100 mm with a digital resolution of 18.5 pixels/mm. Sequences of images are also recorded at 20 Hz in frame-straddling mode (pulse separation time 1 ms) for a total time of 25 s to have statistically converged measurements.

The volumetric light intensity reconstruction is performed following the of Multiplicative Algebraic Reconstruction Technique algorithm (MART, Hermann and Lent, 1976) by LaVision software *Davis* 8. A three-dimensional mapping function from image-space to physical object-space is generated by imaging a calibration target. The initial experimental errors due to system calibration are estimated at approximately 0.5 pixels by the disparity vector field. The misalignment is reduced to less than 0.05 pixels making use of the *self-calibration* technique (Wieneke, 2008). The raw images are pre-processed with subtraction of the minimum intensity at each pixel for the entire sequence, followed by a

subtraction of the local minimum over a kernel of 31x31 pixels. The MART algorithm is applied with four iterations. At the given particle image density, despite the radial decrease and axial increase (section 3.2), the use of 3-camera tomographic system leads to rather accurate 3D object reconstructions with a reconstruction quality *Q* above 0.75 (Elsinga *et al*., 2006).

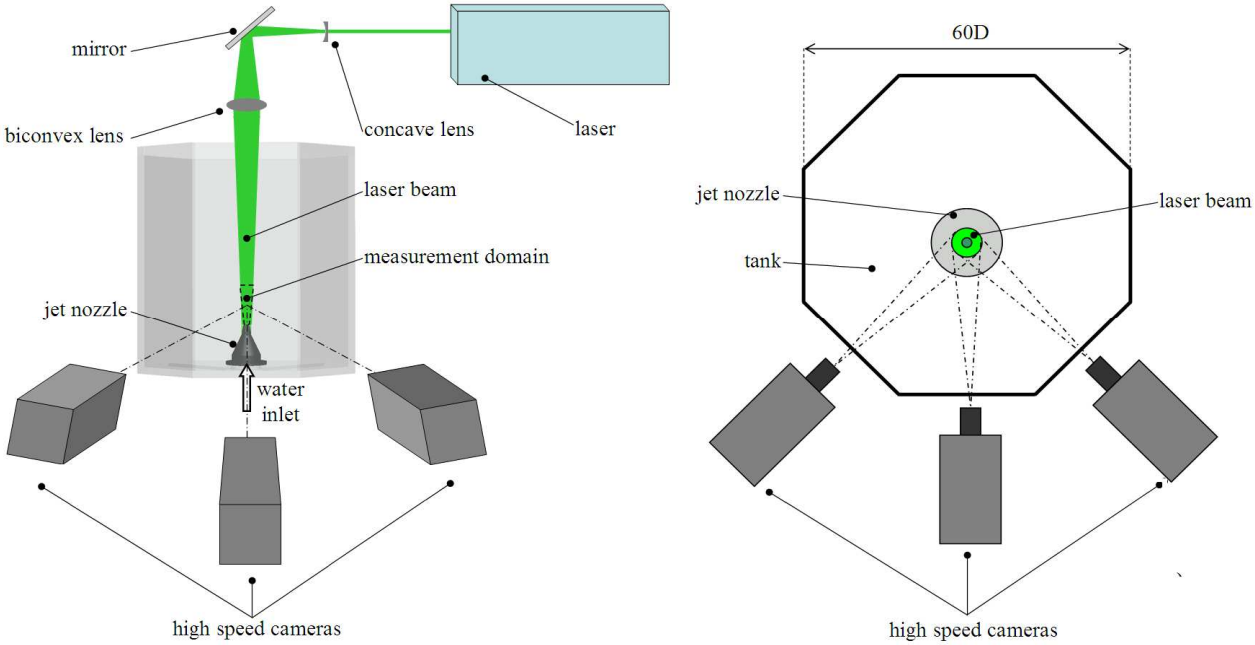

Figure 1 Schematic view of illumination and imaging in the tomographic experiment (left); top view of the system (right).

Table 1. Experimental settings for time-resolved measurements

Seeding material	polyamide particles diameter: 56 [µm] concentration : 0.65 [particles/mm3]
Illumination	Quantronix Darwin-Duo Nd-YLF laser (2 x 25mJ@1 kHz)
Recording device	3 Imager pro HS 4M cameras (2016 x 2016 pixels@ 1.3 kHz) 11 µ pixel pitch
Recording method	double frame/single exposure continuou mode
Optical arrangement	Nikon objectives (f =105mm; f#=22) field of view 5D x 10D
Acquisition frequency	1 kHz
Time of acquisition	2 s

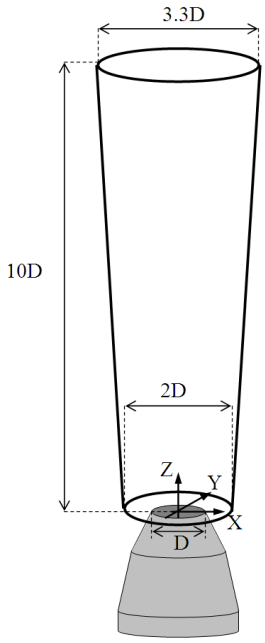

Figure 2. Details of the measurement domain and coordinate system.

The illuminated volume is discretized with 660 x 660 x 2000 voxels resulting in a digital resolution of 20 voxels/mm (voxel pitch of 50 μm). Following Elsinga *et al*. (2006), the accuracy of the reconstruction is evaluated *a-posteriori* comparing the intensity of reconstructed particles in the illuminated region with that of *ghost particles* produced in the immediate surroundings of the illuminated domain. A signal-to-noise ratio may be defined as the reconstructed particles intensity inside the illuminated area versus that reconstructed outside. In the present experiment, the intensity distribution of the laser light is approximately Gaussian and the light is concentrated in the conical volume shown in Figure 2 where the signal-to-noise ratio is higher than 4.

The three-dimensional particle field motion is computed by Volume Deformation Iterative Multigrid (VODIM) technique (Scarano and Poelma, 2009) with a final interrogation volume of 40x40x40 voxels (2x2x2 mm^3) with an overlap between adjacent interrogation boxes of 75%, leading to a vector pitch of 0.5 mm. Correlation averaging technique over three subsequent object-pairs is applied to have higher signal-to-noise ratio and higher measurement precision in time-resolved measurements (Scarano *et al*. 2010) Data processing is performed on a dual quad-core Intel *Xeon* processor at 2.83 GHz with 8 GB RAM memory requiring, respectively, 1 h and 40 min for the reconstruction of a pair of objects and 2 h for the 3D cross-correlation.

The suppression of the spatio-temporal noisy fluctuations is obtained by applying the second order polynomial least squares regression (Scarano and Poelma, 2009) with a kernel size of 5 grid nodes in space (2 mm^3), corresponding to the interrogation box size, and 7 time steps (6 ms). The velocity is affected by 2% precision error with respect to the particle displacement at the jet exit of 10 voxels; the vorticity, in contrast, is subjected to a precision error of 3% with respect to the vorticity magnitude at the core of a shed vortex (0.25 voxels/voxel). For details on the correlation technique, filtering method and spatio-temporal resolution of the data, the reader is referred to Violato and Scarano (2011).

4. RESULTS

4.1 UNSTEADY FLOW BEHAVIOR

In in the region near to the nozzle exit (Z/D=0 and Z/D=5.5), toroidal vortices shed and pair with a Strouhal number $St=fD/W_j$ of 0.72 and 0.36, respectively. The characteristic pulsatile motion of shedding and pairing leads to the growth of azimuthal instabilities and the formation counter-rotating pairs of streamwise vortices of radial and axial vorticity . The instantaneous flow organization is shown in Figure 3 where toroidal vortices are identified by iso-surfaces of azimuthal vorticity $\omega_\theta D/W_j$ whereas the three-dimensional development is visualized by the axial vorticity components $\omega_z D/W_j$. The reader is referred to Violato and Scarano (2011) where more detailed descriptions of the vortex dynamics in the region near to the nozzle are available. The potential core extends along the first 6.5 diameters. In the region beyond the end of the potential core (Z/D>6) ring vortices are not detected and streamwise filaments of $\omega_r D/W_j$ and $\omega_z D/W_j$ are dominant.

The pattern evolution during the breakdown of a toroidal vortex is shown in the temporal sequence of Figure 4, where the iso-surface λ_2=-0.8 identifying the vortices are color-coded by the instantaneous axial velocity W/W_j and are shown between R/D=0 and R/D=1. The decay of the azimuthal coherence of toroidal structures begins after pairing with the growth of four in-plane (see label "P", t=0) and four out-of-plane azimuthal instabilities. With the growth of in-plane azimuthal instabilities, portions of the vortex ring (see labels "P") are stretched towards the jet axis (0<t<1.26), where the axial velocity is larger (W/W_j=1). Due to the asymmetric distribution of W, regions "P" are then ejected and tilted along the jet axis (1.68<t<2.1), producing axial stretching and, ultimately, the disruption of the toroidal shape (Z/D=5.8 and 6.5). By the end of the potential core, the characteristic axial and radial velocity fluctuations are w'/W_j=0.16 and v_r'/W_j =0.14, 30% smaller than those observed for the pairing process. In contrast, azimuthal velocity component reaches peak activity of 0.11, which is about twice that at pairing. Vortex portions originated from low-axial velocity regions gradually disrupt into smaller structure of "C" shape (see label "C", 1.68<t<2.52), whereas those originated from region "P" form an angle of 30-45 degrees with the jet axis (2.52<t<2.94).

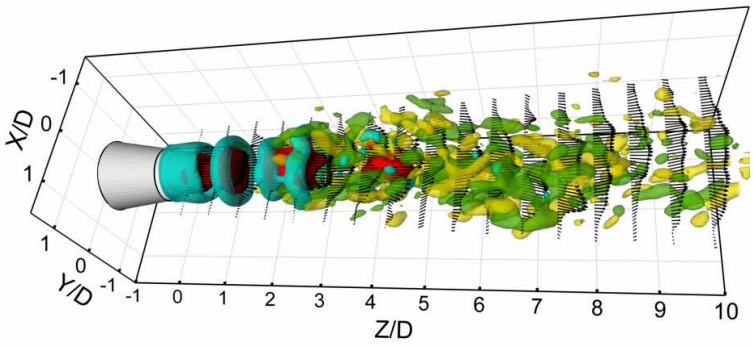

Figure 3 Instantaneous vortex pattern in the circular jet during pairing. Velocity vector slice in the axial plane. Iso-surfaces of axial velocity W/W_j=1.05 (red). Iso-surface of vorticity components $\omega_\theta D/W_j$ =4 (cyan), $\omega_z D/W_j$ =-1.2 (green) and 1.2 (yellow).

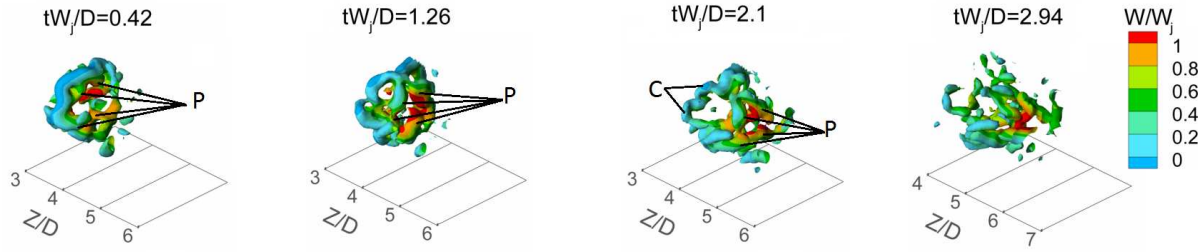

Figure 4 Time sequence visualization of vortex ring breakdown. Iso-surface λ_2=-0.8 color coded with axial velocity component W/W_j. Time separation between snapshots $\Delta tW_j/D$=0.42.

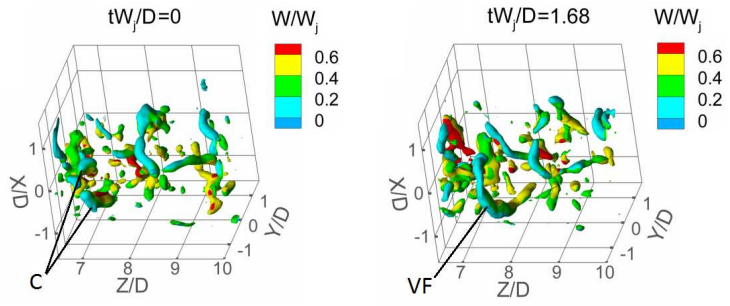

Figure 5 Time sequence visualization of vortices after breakdown. Iso-surface λ_2=-0.5 color coded with W/W_j.

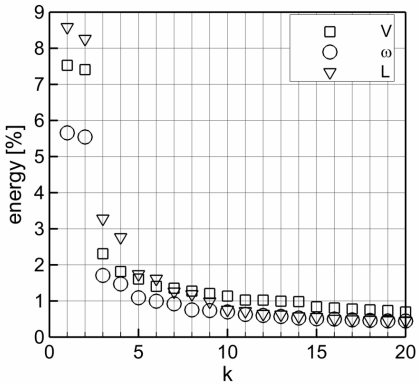

Figure 6 Energy distribution across first 20 modes.

Downstream the potential core (7<*Z/D*<10), vortex rings are replaced by a fully three-dimensional regime where the most recurrent patterns are vortex filaments with scattered orientation (Figure 5). The decay of the vortex coherence is faster between 0<*R/D*<0.8 where the axial velocity is characterized by flow patches of maximum axial velocity

W/W_j=0.6, and velocity fluctuations w'/W_j, v_r'/W_j and v_t'/W_j of comparable magnitude (0.1-0.12). By contrast, in the periphery of the jet (0.8<R/D<1.6), where fluctuations are about 50% smaller, "C" structures (tW_j/D=0) tend to re-organize into filaments "VF" (tW_j/D=1.68). "VF" structures are typically oriented along the azimuthal direction and have a characteristic length ranging between 1 to 2 jet diameters, based on iso-surface λ_2=-0.5. The advection axial velocity is 0.2. They induces fluid engulfment on the trailing side and ejection on the leading one, with peaks of instantaneous radial velocity of 0.1. The typical life-time of the "VF" is $\Delta tW_j/D$=6 after which they breakdown into sub-structures between Z/D=9 and 10.

4.2 MODAL DECOMPOSITION

POD analysis is applied to inspect the three-dimensional patterns of velocity, vorticity and Lamb vector fields in the region of jet core collapse. The analysis is conducted using a sequence of 500 velocity snapshots which corresponds to an observation length of 1000 jet diameters. The distributions of energy across the first 20 POD modes are illustrated in Figure 6. Mode #1 and 2# of the velocity correspond to 7.5% and 7.4% of the total kinetic energy, whereas far less enstrophy corresponds to vorticity mode #1 and #2 (5.7% and 5.6%). The most efficient decomposition seems that on the Lamb vector where mode #1 and 2# respectively capture 8.6% and 8.3% of the related energy. However, quantitative comparisons between the decompositions of velocity, vorticity and Lamb vector are possible only if referred to the same norm.

The first 10 velocity modes, which corresponds to 27.5% of the kinetic energy, there are pulsatile modes (3 and 8) and pairs (1 and 2, 4 and 5, 6 and 7, 9 and 10) phase shifted of π/2 in the axial direction describing travelling waves. For conciseness, Figure 7 shows the iso-surfaces of W/W_j,V_r/W_j, and V_θ/W_j of one mode for each pair. Mode #1 and #2 describe travelling toroidal vortices that are formed after pairing (not illustrated). In mode #4 and #5, across the end of the potential core (6<Z/D<8), the intertwining between the region of positive and negative W/W_j describe a *helical* motion (Iqbal and Thomas, 2007). Further downstream (Z/D>8), instead, they describe a *flapping* motion (Lynch and Thurow, 2009). The aforementioned motions are coupled with a *wave-like* motion (V_r/W_j) and a periodic *twisting* (V_θ/W_j) that have 4 jet diameters of spatial frequency. Mode #6 and #7 describe travelling toroidal vortices before pairing (not illustrated). Mode #9 and #10, where two filaments of positive W/W_j and two filaments of negative W/W_j are phased shifted of π/2 on the plane normal to the jet axis describe a *precession* motion. This is coupled with a *wave-like* motion (V_r/W_j) and a periodic *twisting* (V_θ/W_j) that are similar to those observed in mode #4 and #5. Mode #3 and mode #8 (not illustrated) are characterized by the axial development of four filaments of W/W_j and V_r/W_j, two of positive sign at π/2 with two of negative sign. They describe axial and radial pulsatile motions (4<Z/D<9) with a phase shift of about 45 degrees in the azimuthal direction.

POD analysis is now applied to the vorticity fields to describe the large coherent structures that develop in the jet. In the first 10 velocity modes, which corresponds to 20% of the flow enstrophy energy, there are pairs (1 and 2, 3 and 4, 5 and 6, 8 and 9) phase shifted of π/2 in the axial direction describing travelling waves. Travelling ring vortices after pairing are described by mode #1 and mode #2 (Figure 8) which are the most energetic (5.7% and 5.6% of the total energy), as found from the velocity decomposition. The patterns of three-dimensional coherence, which is peculiar of the process that lead to the breakdown of toroidal vortices, is illustrated by iso-surfaces of radial and axial components of the vorticity modes, $\omega_r D/W_j$ and $\omega_z D/W_j$, as well as by cross-sectional iso-contours plots of the same quantities. Mode #1 and 2# show that the motion of vortex rings after pairing (see isosurfaces of $\omega_\theta D/W_j$) is accompanied by travelling waves of $\omega_r D/W_j$ and $\omega_z D/W_j$ that develop across the end of the potential core. They show a characteristic inclination of 40-45 degrees to the jet axis for Z/D>4.5 (see dashed lines) and phase opposition on the plane normal to the jet axis (see iso-contour plots at Z/D=5.5). Similar patterns are observed in mode #5 and #6 (not illustrated) which are rotated of π/2 around the jet axis. Pulsatile modes #7 and #10 show four pairs of counter-rotating streamwise filaments of $\omega_r D/W_j$ and $\omega_\theta D/W_j$ that develop across the region of vortex breakdown between Z/D=3.5 and Z/D=8.

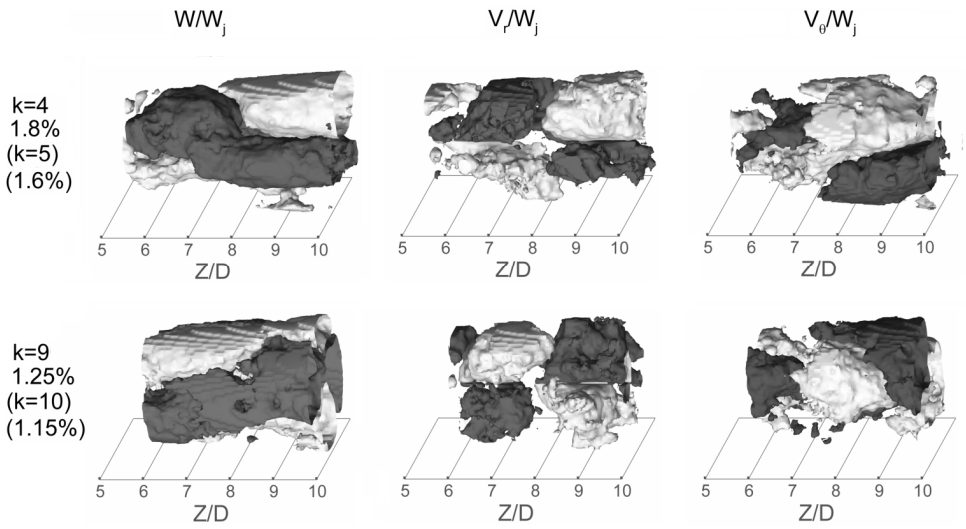

Figure 7 POD modes of velocity describing travelling waves. Between brackets mode number and energy of the coupled mode. Positive (light grey) and negative (dark grey) iso-surfaces of W/W_j (left), V_r/Wj (centre) and V_θ/Wj (right)

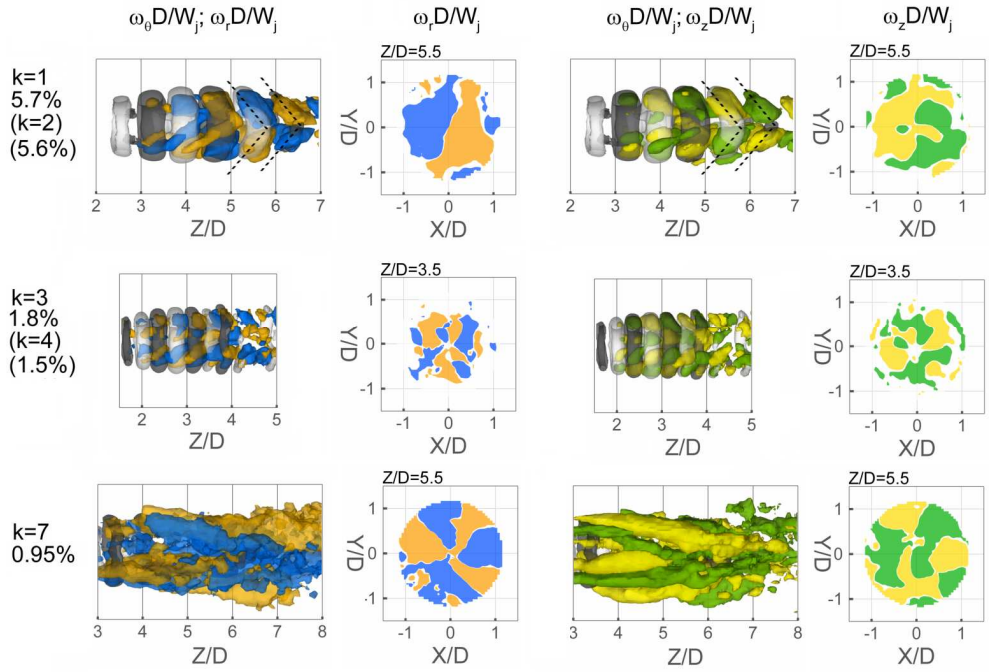

Figure 8 POD modes of vorticity. Between brackets mode number and energy of the coupled mode. Left: iso-surfaces of $\omega_\theta D/W_j$ (positive in light grey; negative in dark grey) and $\omega_r D/W_j$ (positive in orange and negative in blue) and cross-sectional iso-contour of $\omega_r D/W_j$. Right: iso-surfaces of $\omega_\theta D/W_j$ (positive in light grey; negative in dark grey) and $\omega_z D/W_j$ (positive in yellow and negative in green) and cross-sectional iso-contour of $\omega_z D/W_j$ with iso-line $\omega_\theta D/W_j$.

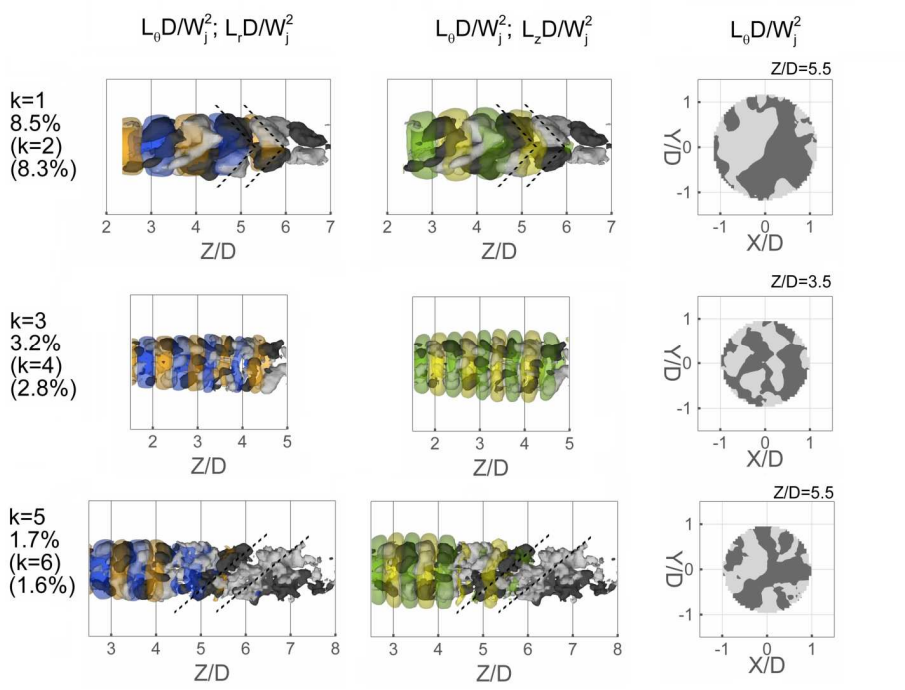

Figure 9 POD modes of Lamb vector describing travelling waves. Between brackets mode number and energy of the coupled mode. Left: iso-surfaces of $L_\theta D/W_j$ (positive in light grey; negative in dark grey) and $L_r D/W_j$ (positive in orange and negative in blue); centre: iso-surfaces of $L_\theta D/W_j$ (positive in light grey; negative in dark grey) and $L_z D/W_j$ (positive in yellow and negative in green); right: cross-sectional iso-contour of $L_\theta D/W_j$.

The POD analysis of the Lamb vector, which in Powell's aeroacoustic analogy accounts for the flow state, shows the first 10 modes capturing 30.3% of the total energy content. Travelling waves are described by the first 4 pairs of modes which are illustrated in Figure 9. While in the vorticity modes toroidal vortices were described by the azimuthal vorticity component (Figure 8), in the Lamb vector modes the azimuthal coherence is described by the radial and the axial components $L_r D/W_j$ and $L_z D/W_j$. Three-dimensional coherence is instead described by the azimuthal component $L_\theta D/W_j$ (Figure 9). Mode #1 and mode #2 of the Lamb vector describe the motion of toroidal vortices formed after pairing and the presence of a three-dimensional disturbance (see isosurface $L_\theta D/W_j$) that develop across the end of the potential core. This disturbance grows with a characteristic 40-45 degrees inclination to the jet axis, similarly to the waves $\omega_r D/W_j$ and $\omega_z D/W_j$ observed in vorticity modes #1, #2, #5 and #6. In the region between Z/D=2.5 and 5, mode #3 and #4 describes travelling toroidal vortices after shedding as observed for the vorticity decomposition. The motion is combined with travelling wave of $L_\theta D/W_j$ that show an azimuthal distribution with a wave number k=4, similarly to that observed in mode #3 and #4 for the radial and axial component of the vorticity (see cross-sectional plots). Mode #5 and #6, as well as mode #7 and #8 (not illustrated), show a travelling wave of $L_\theta D/W_j$ characterized by three main filaments of positive and negative sign that swirl around the jet axis with an angle of 40-45 degrees to the jet axis in the region across the end of the potential core ($5<Z/D<7$). Pulsatile modes #9 and #10 (not illustrated) show 6 main pairs of streamwise filaments of $L_\theta D/W_j$ coherence that develop until the region of vortex breakdown (Z/D=5.5) and then merge into a main pair (Z/D=7.5). This, in mode #10, is rotated of about $\pi/2$ around the jet axis with respect to mode #9.

4.3 ACOUSTIC SOURCE CHARACTERIZATION

The phenomenological aspects of the large-scale flow fluctuations have been so far discussed in relation to the unsteady and three-dimensional behavior at transition. Although the current experiment does not enable to cover the entire region

of acoustic production, neither to resolve all the spatial scales at which acoustic fluctuations are produced, the role of coherent vortices, i.e. vortex rings, streamwise vortices, in the local activity of acoustic source can be explored.

For low Mach numbers and compact source regions, with no external force field and neglecting viscous-thermal effects, the far-field solution of Powell's analogy (Powell, 1964) reads as

$$p'(\mathbf{x},t) = -\frac{\rho_0}{4\pi c_0^2 |\mathbf{x}|^3}\frac{\partial^2}{\partial t^2}\iiint_V (\mathbf{x}\cdot\mathbf{y})\,\mathbf{x}\cdot\mathbf{L}\big|_{t^*} d^3\mathbf{y} \qquad (8)$$

where **x** is the listener position vector, **y** is the source position vector, **L** is the Lamb vector evaluated at the retarded time $t^* = t - |\mathbf{x}|/c_0$ and V is the three-dimensional domain. For the linear property of the integral function, the second time derivative can be applied to the Lamb vector. A survey on the spatio-temporal pattern of

$$\ddot{\mathrm{L}} = \left|\frac{\partial^2}{\partial t^2}\mathbf{L}\right| = \left[\left(\frac{\partial^2}{\partial t^2}L_X\right)^2 + \left(\frac{\partial^2}{\partial t^2}L_Y\right)^2 + \left(\frac{\partial^2}{\partial t^2}L_Z\right)^2\right]^{1/2} \qquad (9)$$

is discussed in relation large-scale structures that are identified by the λ_2-criterion.

Figure 10 shows that the production of $\ddot{\mathrm{L}}$ corresponds to vortex rings downstream of Z/D=3 ("3") especially at pairing ("1" and "2"). Peak activity of 50 is associated with streamwise structures ("S"). The temporal sequence of Figure 11 illustrates the vortex patterns evolution (λ_2 iso-surfaces) and the corresponding acoustic source field (iso-surfaces of $\ddot{\mathrm{L}}$) during the breakdown process of a vortex-ring structure. Before breakdown (tW_j/D=0), the acoustic source shows a toroidal configuration corresponding to the vortex ring, with peak activity associated with the azimuthal instabilities. Subsequently, during the loss of azimuthal coherence (0.84<tW_j/D<1.68), the acoustic source is more pronounced in the region closer to the jet axis, where portions "P" of the vortex ring are ejected and tilted along the jet axis (Figure 4). On the other hand, the rupture of the vortex into "C" structures does not seem to cause acoustic emissions. Beyond the end of the potential core, the source activity rapidly decreases.

A statistical distribution of the source along the jet axis is illustrated in Figure 12, which shows the average of $\ddot{\mathrm{L}}$ over the entire observation time and along the azimuthal direction between R/D=0 and 1 ($\langle\ddot{\mathrm{L}}\rangle$). Peak activity of $\langle\ddot{\mathrm{L}}\rangle$ is observed between Z/D=5.5 and 6 where the portions "P" of vortex rings are stretched, tilted and then axially ejected yielding the disruption of the toroidal coherence. Beyond the end of the potential core, $\langle\ddot{\mathrm{L}}\rangle$ decreases to 3.5, which is comparable to the activity in the region upstream pairing (Z/D=2.5).

5 CONCLUSIONS

The three-dimensional behavior of flow transition in circular jet at Re=5000 has been studied by experiments conducted in a tailored-water jet facility with TR-TOMO PIV. State-of-the-art experimental capabilities are employed to perform experiments on volumetric domain 10 jet diameters long. The flow exhibits a pulsatile motion according to the shedding and pairing of vortex rings, followed by the formation of counter-rotating pairs of streamwise vortices and the growth azimuthal instabilities. These culminate in the breakdown of vortex ring by the end of the potential core as a consequence of the abrupt axial ejection of the azimuthal humps of the ring structure.

POD analysis is conducted to inspect the three-dimensional patterns at transition. By the end of the potential core, the most energetic modes of velocity show helical and precession motion of the jet core, whereas the those of vorticity reveal a characteristic 45 degrees orientation to the jet axis of the radial and the axial components. Lamb vector modes show a similar orientation for the azimuthal component.

The relation between coherent flow structures and the instantaneous acoustic production is investigated recalling Powell's analogy. Noise sources are characterized by the second time derivative of the Lamb vector. Its spatio-temporal evolution is visually compared to that of the vortices, which are detected by λ_2-criterion, to identify large-scale patterns

involved in the acoustic generation. Acoustic source is associated with the vortex pairing, azimuthal instabilities and streamwise filaments. The vortex ring breakdown shows the most intense source activity.

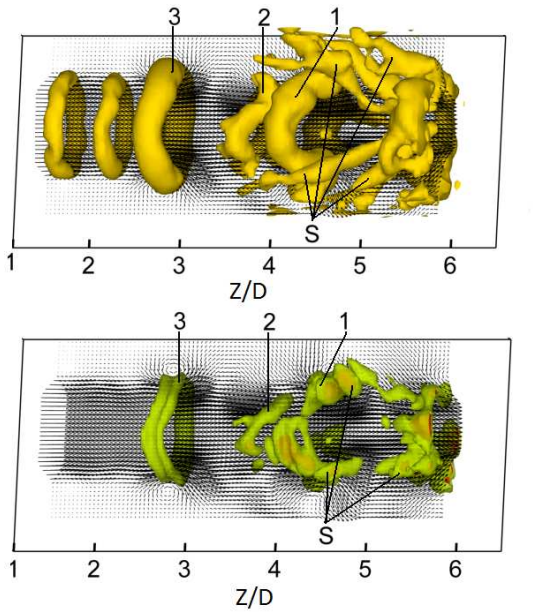

Figure 10 Source activity of vortex rings at pairing. Top: iso-surfaces λ_2=-0.8 (yellow); Bottom: iso-surfaces $\ddot{L}$ =30 (green) and $\ddot{L}$ =50 (red).

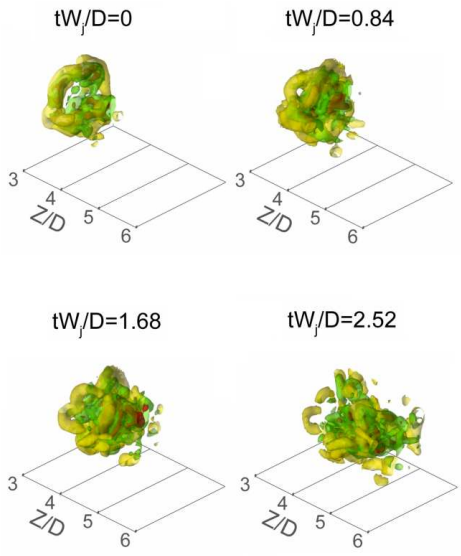

Figure 11 Source activity during vortex ring breakdown (iso-surfaces λ_2=-0.8 in yellow) with acoustic source (iso-surfaces $\ddot{L}$ =30 in green and $\ddot{L}$ =50 in red).

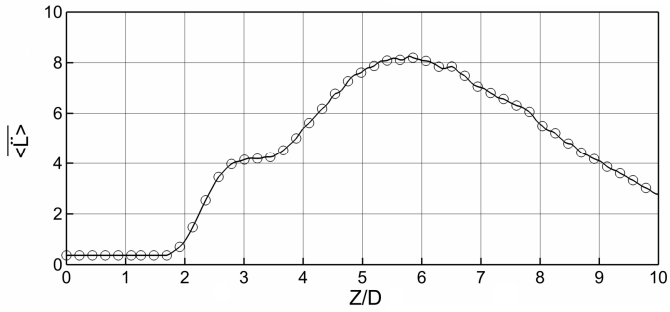

Figure 12 Space-time average of $\ddot{L}$

ACKNOWLEDGMENTS

The authors kindly acknowledge LaVision GmbH and Prof. Piero Colonna for providing the CMOS cameras and Dr. Andrea Ianiro for the realization of the experiments. This work was conducted as part of the FLOVIST project (Flow Visualization Inspired Aeroacoustics with Time Resolved Tomographic Particle Image Velocimetry), funded by the European Research Council (ERC), grant no 202887.

REFERENCES

Berkooz, G, Holmes, P and Lumley JL (1993). The proper orthogonal decomposition in the analysis of turbulent flows. Annu. Rev. Fluid Mech., Vol. 25, pp. 539-575.

Crow S, Champagne F (1971). Orderly structure in jet turbulence. Journal of Fluid Mechanics 48:547–591.

Dimotakis PE, Miake-Lye RC, Papantoiou DA (1983). Structure dynamics of round turbulent jets. Physics of Fluids 26:3185-3192.

Elsinga GE, Scarano F, Wieneke B, van Oudheusden BW (2006). Tomographic particle image velocimetry. Experiment Fluids 41:933–947.

Hermann GT and Lent A (1976). Iterative reconstruction algorithms. Comput. Biol. MA. Pergamm Press 1976. Vol. 6. pp. 273-294

Hussain F, Zaman KBMQ (1981). The preferred mode of the axisymmetric jet. Journal of Fluid Mechanics. 110:39-71.

Iqbal MO and Thomas FO (2007). Coherent structure in a turbulent jet via a vector implementation of the proper orthogonal decomposition. Journal of Fluid Mechanics 571: 281-326.

Jordan P and Gervais Y (2008). Subsonic jet aeroacoustics: associating experiment, modelling and simulation. Experiments in Fluids DOI 10.1007/s00348-007-0395-y.

Jeong J, Hussain F (1995). On the identification of a vortex. Journal of Fluid Mechanics 285:69–94.

Kostas J, Soria J, Chong MS (2005) A comparison between snapshot POD analysis of PIV velocity and vorticity data Experiments in Fluids 38:146-160.

Liepmann D, Gharib M (1992). The role of streamwise vorticity in the near field entrainment of round jets. Journal of Fluid Mechanics 245:643–668.

Lynch KP, Thurow BS (2009). POD analysis of 3d-flow visualization images of a circular jet with Reynolds number 9500. 39th Fluid Dynamics Conference, San Antonio, Texas, USA.

Morris SC (2011). Shear layer instabilities: particle image velocimetry measurements and implications for acoustics. Annual review of Fluid Mechanics 43: 529-550.

Powell A (1964). Theory of vortex sound. Journal the Acoustical Society of America 36, 177-195.

Scarano F, Poelma C (2009). Three-dimensional vorticity patterns of cylinder wakes. Experiment Fluids 47:69–83.

Schram K, Taubitz S, Anthoine J, Hirschberg A (2005). Theoretical/empirical prediction and measurement of the sound produced by vortex pairing in a low Mach number jet. Journal of Sound and Vibration 281:171–187.

Seiner JM (1999). Jet noise source measurements using PIV. 5th AIAA/CEAS Aeroacoustic conference, Bellevue (Great Seattle), USA.

Sirovich L (1987). Turbulence and the dynamics of coherent structures. Part 1: Coherent structures. Quarterly of App. Math., Vol. XLV, pp. 561-571.

Violato D, Scarano F (2011) Three-dimensional evolution of flow structures in transitional circular and chevron jets. Physics of Fluids, DOI: 10.1063/1.3665141.

Wieneke B (2008). Volume self-calibration for 3D particle image velocimetry. Experiment Fluids 45:549–556.

Yule AJ (1978). Large structure in the mixing layer of a round jet. Journal Fluid Mechanics 89:413-432.